Vacuum Ultraviolet Single Photon Ionization and Decomposition of 2-Aminopropionitrile in Astrophysical Objects

Helgi Rafn Hrodmarsson[1] , Martin Schwell[1] , Nicolas Fray[1] , Jean-Claude Guillemin[2] , Majdi Hochlaf[3] , and Emilie-Laure Zins[4]

[1] Univ Paris Est Creteil and Université Paris Cité, CNRS, LISA, F-94010 Créteil, France; martin.schwell@lisa.ipsl.fr
[2] Univ Rennes, École Nationale Supérieure de Chimie de Rennes, CNRS, ISCR-UMR6226, F-35000 Rennes, France
[3] Université Gustave Eiffel, COSYS/IMSE, 5 Bd Descartes F-77454, Champs sur Marne, France
[4] MONARIS UMR 8233 CNRS, Sorbonne Université, 4 place Jussieu, F-75252 Paris Cedex 5, France

Abstract

The molecule 2-aminopropionitrile (2-APN; $H_3CCH(NH_2)CN$) is a chiral precursor of the amino acid alanine and could play an important role in the emergence of the homochirality of life. To date, 2-APN has not yet been detected in the interstellar medium. To address the question of its absence, possibly through destruction by vacuum ultraviolet radiation in astrophysical media, we studied its photoionization and dissociative photoionization in the 9–14 eV (89–137 nm) energy range using photoelectron–photoion coincidence spectroscopy with velocity map imaging. Density functional theory calculations were performed at the PBE0/aug-cc-pVTZ level to determine structures for the various cationic fragments identified experimentally. Their appearance energies were calculated. The adiabatic ionization energy (AIE) of 2-APN is $AIE = (9.85\pm0.01)$ eV and the appearance energy (AE) of the major fragment ion $N{\equiv}CC(H)NH_2^+$ is $AE = (10.57\pm0.01)$ eV. Both ions, 2-APN$^+$ and $N{\equiv}CC(H)NH_2^+$, make up more than 90% of the formed ions. $N{\equiv}CC(H)NH_2^+$, an isomer of the protonated HCN dimer, is also formed with high yield in the dissociative photoionization of aminoacetonitrile (NH_2CH_2CN), another α-aminonitrile observed in Sgr B2(N). Photoion yield spectra have been calibrated to absolute ionization cross sections. From these, we derive photoionization rates in several typical radiation fields relevant to different astrophysical objects. The rates show that, under almost all explored radiation fields, dissociative ionization is the dominant pathway for photoionization, leading to the loss of a methyl group (CH_3) to form the planar thermodynamically stable amino cyano methylidynium ion $N{\equiv}CC(H)NH_2^+$. The observed absence of 2-APN in Sgr B2 could thus be due to dominant dissociative photoionization.

1. Introduction

In recent years, the detection rate of molecules in the interstellar medium (ISM) has been swiftly accelerating (Endres et al. 2016). This is in large part thanks to significant advances in detection techniques and astronomical data processing that are being pioneered by, e.g., the QUIJOTE project, which is now detecting molecules with mK sensitivity (Agúndez et al. 2015; Cernicharo et al. 2021), and the GOTHAM project, which has been pioneering a spectral stacking method to significantly enhance the signal-to-noise ratio of astronomical spectra, thus facilitating detections of astronomically important molecules such as the first polycyclic aromatic hydrocarbons (Burkhardt et al. 2021; Cernicharo et al. 2021; McGuire et al. 2021) and the first chiral molecule, propylene oxide, to be detected in the ISM (McGuire et al. 2016).

The origin of molecular chirality in living systems is one of the most intriguing mysteries in science (Mason 1986; Bonner 1995; Guijarro & Yus 2007). The favoritism of specific combinations of enantiomers raises a multitude of questions regarding the chemistry of the primitive universe and in particular on nascent Earth that eventually spawned the first living organisms (Evans et al. 2012).

Chirality has indeed been found to be induced in the synthesis of amino acids in interstellar ice analogs using circularly polarized UV light (UV-cpl; de Marcellus et al. 2011; Nuevo et al. 2006; Takano et al. 2007). Although it is unclear whether UV-cpl originally helped generate a universal enantiomeric excess by means of photolysis, asymmetric isomerization, asymmetric photosynthesis, or a combination of these processes, it is generally accepted that the initial spawning of molecular handedness occurred in interstellar or circumstellar environments (Bailey 1998; Fukue et al. 2010).

Astronomical searches for the smallest amino acid, glycine, already spawned a massive debate ending with the retraction of glycine's detection in the ISM (Snyder et al. 2005; Cunningham et al. 2007; Jones et al. 2007). Nevertheless, the search for this amino acid and its isomers is still a very active field. Very recently, Rivilla et al. (2023) successfully detected glycolamide ($H_2NC(O)CH_2OH$), an isomer of glycine. They deduced a molecular abundance of glycolamide with respect to H_2 of 5.5×10^{-11}. Glycine, if present in the ISM, should have an even smaller abundance.

The nondetection of glycine in turn sparked searches for so-called prochiral molecules, meaning that they can be converted to chiral molecules in a single step (Askeland et al. 2006; Cole et al. 2007). In the literature, there are competing theories concerning the formation of the first amino acids from already chiral precursors. A very promising strategy involves the detection of the precursors of amino acids as predicted by such
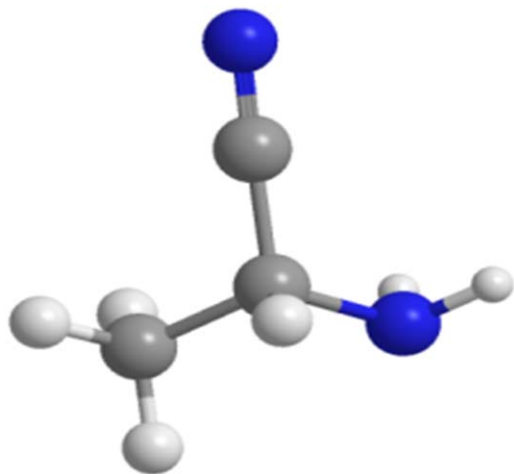
Figure 1. Structure of 2-aminopropionitrile (2-APN).

scenarios (e.g., the Strecker reaction). Among the most prominent of such molecules is 2-aminopropionitrile (hereafter called 2-APN but also called α-aminopropionitrile in the literature), with the elemental formula $C_3H_6N_2$. With a chiral carbon in the α-position (see Figure 1), 2-APN can be converted to the amino acid α-alanine by means of hydrolysis (Bejaud et al. 1975). It has been found in arc-discharge experiments of methane and ammonia mixtures as representing the constituents of primitive atmospheres (Ponnamperuma & Woeller 1967). Its physical properties are still relatively unknown, but it has been shown to possess three thermo-dynamically stable neutral conformers very close in energy (Møllendal et al. 2012). At 800°C, 2-APN thermally decom-poses into HCN and $CH_3CH{=}NH$ (Guillemin & Denis 1988).

Much effort has been devoted to detecting 2-APN in the ISM but so far without success. Møllendal et al. (2012) measured the rotational spectrum of 2-APN and searched for the compound in Sgr B2(N). They concluded that 2-APN is at least 1.8 times less abundant than aminoacetonitrile (AAN), which had been detected previously in Sgr B2(N) (Belloche et al. 2008), and that a simple comparison to the pair of methyl and ethyl cyanide detected toward Sgr B2(N) suggested that 2-APN should be 3.5 times less abundant than AAN, which is consistent with the limit derived by Møllendal et al. (2012). Recent searches for 2-APN (and also for 3 (or β)-APN, which is not chiral) have been performed with the Atacama Large Millimeter/submillimeter Array (ALMA), but only upper abundance limits could be derived (Richard et al. 2018). Note that 2-APN is the methyl homolog of AAN, which has been studied thoroughly earlier by our group in the vacuum ultraviolet (VUV) spectral domain using similar methods to those presented here (Bellili et al. 2015a, 2015b).

There are several reasons why chiral molecules have so far eluded detection in the ISM. One prominent principle that has been helpful for chemical astronomers is the minimum energy principle (MEP). It states that, when considering a particular molecular structure belonging to a set of isomers with the same elemental formula, the ordering of interstellar abundance follows the thermodynamic stability of the respective isomers, with the isomer lowest in energy being highest in observed abundance. This principle is obeyed in many astrophysical objects and for many isomers, as outlined by Lattelais et al. (2009, 2010). About 90% of the molecules detected in the ISM comprising more than two atoms satisfy this principle, which is

not a law. In the case of 2-APN, there are a lot of stable $C_3H_6N_2$ isomers, for example 3-aminopropionitrile, N-methyl-aminoacetonitrile, pyrazoline (all nonchiral), to cite only a few. The exact energetic ordering of stable $C_3H_6N_2$ isomers has been recently studied with ab initio calculations, which indeed have found 2-APN to be the most stable isomer, with 3-APN following close behind, among a total of eight $C_3H_6N_2$ isomers studied (Shoji et al. 2022).

Besides the MEP, other useful guides by which the search for interstellar chiral molecules is conducted include size, rigidity, dipole moment, and their propensity to desorb from interstellar ices (Ellinger et al. 2020). What is missing from this list is molecular VUV photostability, i.e., how the molecule interacts with radiation in the VUV range. Some efforts have been made to understand the VUV photostability of astro-biologically relevant molecules, and it has been found that nitriles photodegraded 5–10 times more slowly than their corresponding acids (Bernstein et al. 2004), but more detailed insights into the multitudes of molecule detections (and nondetections) are still missing.

To further understand molecule nondetections and upper limits, it is important to thoroughly understand how these molecules interact with VUV radiation, as they can be ionized in the ISM, circumstellar disks, molecular clouds, etc. Thus, understanding the photoionization and dissociative photoioni-zation pathways can help postulate how likely or unlikely it is to find the molecules in question or whether searching for any fragments formed by dissociative ionization would provide a proxy for the molecule's interstellar presence. We note that ionization and destruction of molecules can also be caused by cosmic rays and energetic collisions with other particles. All these processes must be deciphered by adequate models of respective astrophysical objects.

Theoretical work has been performed addressing chirality inversion routes of 2-APN (Kaur & Vikas 2015) but, to the best of our knowledge, no VUV spectrum or any other photophysical data in this spectral domain have been reported in the literature. Here, we present for the first time data pertaining to the combined experimental and theoretical investigation of VUV photoioniza-tion of 2-APN and fragments formed via its dissociative ionization. This work continues the recent synergistic approach of experiment and theory dedicated to characterizing astroche-mically and astrobiologically relevant molecules (Bellili et al. 2014, 2015a, 2015b, 2019; Derbali et al. 2019, 2020).

2. Methods

2.1. Experiment

Experiments were performed at the DESIRS VUV beamline at the SOLEIL synchrotron in Saint-Aubin, France (Nahon et al. 2012). Horizontally polarized radiation in the 7–14 eV range was generated by an undulator (OPHELIE 2) (Marcouille et al. 2007) from which the radiation passed through a gas filter filled with argon. This was done to suppress higher harmonics from the undulator by four to five orders of magnitude. The photon beam was dispersed by a 6.65 m normal incidence monochromator using its 200 grooves mm^{-1} grating. The photon flux of the resulting beam was between 10^{12} and 10^{13} photons s^{-1} and was directed into the beamline end station where the SAPHIRS chamber is located (Tang et al. 2015). Coupled to SAPHIRS is the DELICIOUS III double-imaging photoion photoelectron coincidence (i^2PEPICO) in which the

synchrotron radiation intersected with a molecular beam under a right angle (Garcia et al. 2013). The generated photoelectrons and photoions were accelerated in opposite directions with a DC electric field with a velocity map imaging spectrometer on the electron side and a modified Wiley McLaren time-of-flight 3D momentum imaging spectrometer on the ion side. This setup allows a PEPICO scheme to be employed, mass-tagging the recorded electron images and eliminating any spurious background compounds.

The energy resolution (10–40 meV) was a convolution of the photon energy resolution from the monochromator and the electron bandwidth, which is projected from the 2D photoelectron matrix that is constructed by inverting (Garcia et al. 2004) the recorded photoelectron images from an energy scan (Hrodmarsson et al. 2019). This allowed obtaining so-called slow photoelectron spectra (SPES), which give the spectral fingerprints of the cation and its fragments formed from dissociative ionization (Poully et al. 2010; Briant et al. 2012). SPES typically offer a better compromise between the resolution and signal intensity when compared to threshold photoelectron spectra (Baer & Tuckett 2017). The 2-APN was synthesized according to Guillemin & Denis (1988). The procedure gives the racemic mixture that is studied by our group.

2.2. Theory

From a theoretical point of view, we focused on the characterization of molecules, ions, and radicals in their fundamental electronic state. All the calculations were carried out with Gaussian16 software using density functional theory (DFT) with the hybrid functional PBE0 (also known in the literature as "Perdew–Burke–Emzerhof (PBE) hybrid"; Adamo & Barone 1999; Ernzerhof & Scuseria 1999), which uses 25% exact exchange and 75% DFT exchange from the pure PBE functional (Perdew et al. 1996, 1997). The aug-cc-pVTZ triple-ζ Dunning's correlation consistent basis sets augmented with diffuse functions were selected for this study (Dunning 1989; Kendall et al. 1992). Frequency calculations were carried out to check that the optimized structures indeed correspond to local minima in the potential energy surface (no imaginary frequency). All the calculated ionization and dissociation energies include the zero-point energy as well as the anharmonic contributions. To this end, the "anharmonic zero-point energy" calculated in the Gaussian16 software was taken into account. This level of theory was chosen on the basis of comparisons with CCSD reference calculations because of its accuracy in reproducing experimental data at a reasonable computational cost (Pan et al. 2013; Majdi et al. 2015; Derbali et al. 2020; Jarraya et al. 2022). For all the calculations, 2-APN was considered in its most stable conformation. Cartesian coordinates of optimized structures are given in the Appendix Tables A1–A22.

3. Results

Here, we present the combined experimental and theoretical results pertaining to the single photon ionization of 2-APN in the gas phase from the ionization threshold up to 14 eV. As will be shown, experiment and theory complement each other for the analysis of the dissociative photoionization of this molecule.

3.1. Photoionization Time-of-flight Mass Spectra

Figure 2 shows time-of-flight mass spectra with ascending photon energy. At $h\nu = 10.5$ eV (Figure 2(a)), the parent ion m/z

70 is clearly visible, including its ^{13}C isotopologue with its expected abundance ratio ($\sim$3% compared to the parent). We note that we do not see any dimer of 2-APN at m/z 140 in the mass spectra we recorded. A small mass peak at m/z 17 is also visible. The origin of this mass peak can be ionization of NH_3 or dissociative ionization of 2-APN: at 10.5 eV, we are above the ionization energy of NH_3, which is at 10.07 eV (Ruede et al. 1993). From the analysis of the m/z 17 appearance, we can conclude that NH_3 is present as an impurity in the sample but there may be a very minor contribution to the m/z 17 signal from dissociative photoionization from 2-APN according to $C_3H_6N_2 + h\nu \rightarrow NH_3^+ + C_3H_3N$ at higher energies. Comparing the known ionization cross section of ammonia, which is mostly flat between 11.0 and 12.5 eV (Samson et al. 1987), to our measured m/z 17 photoion yield (not shown), we have determined a tentative experimental threshold for NH_3^+ formed by dissociation of 2-APN at 11.5 eV. Other mass peaks with very low intensities are seen at m/z 44, 55, and 69, where the latter appears to be slightly shifted toward the parent ion m/z 70, indicating the slow reaction rate of its formation (see Section 3.3).

At $h\nu = 11$ eV (Figure 2(b)), m/z 55 is clearly visible. This ion is formed via dissociative photoionization of the parent ion. Dissociative reaction pathways will be discussed in the following sections, together with ion yield spectra and SPES. Several other fragment ions with minor intensities are seen at m/z 42, 43, 44, and 69. A small peak located at m/z 46 is from ionized ethanol, used for cleaning procedures of the substance recipient.

At $h\nu = 12.5$ eV (Figure 2(c)), the mass spectrum barely changes in comparison to the mass spectrum at 11.0 eV in Figure 2(b). The intensity of m/z 55 is enhanced while other fragments are more intense too, compared to the parent ion. This is certainly due to higher dissociation yields compared to the lower energy. The main difference is the appearance of O_2^+ (m/z 32) from the ionization of background molecular oxygen.

At $h\nu = 14$ eV (Figure 2(d)), some changes and new masses appear. The ion m/z 69, formed by a H-loss reaction from the parent, is now clearly visible, indicating a faster rate of formation compared to the lower photon energies. The ion m/z 44 turns out to be the strongest in the group of m/z 42, 43, and 44 at this photon energy. An ion at m/z 27 appears with low intensity, probably from dissociative photoionization of 2-APN. The m/z 18 ion is from background water.

3.2. Ion Yield Spectra and Branching Ratio Curves

Figure 3(a) shows ion yield spectra of 2-APN for the parent and all fragment ions formed by dissociative photoionization, also including the total ion yield in blue being the sum of all fragment yield curves. We tentatively scale the ion yield curves to arrive at a cautious estimate of the photoionization cross sections. Given that closed-shell molecules in this size range typically have photoabsorption and photoionization cross sections with maxima between 10 and 100 Mb toward 80 nm (or 15.5 eV) (see Hatano 1999a, 1999b, 2001), we scale the sum of all ions, i.e., the total ion yield, to a maximum of 50 Mb at 14.0 eV. This scaling is very likely correct within an error of an order of magnitude.

Figure 3(b) shows the respective relative branching ratio. The parent ion $C_3H_6N_2^+$ is the only ion observed between its appearance at 10 eV (for a precise determination of its ionization energy, see below) and about 10.5 eV. From this energy on, other ions start appearing (see Figures 3(a) and (b)).
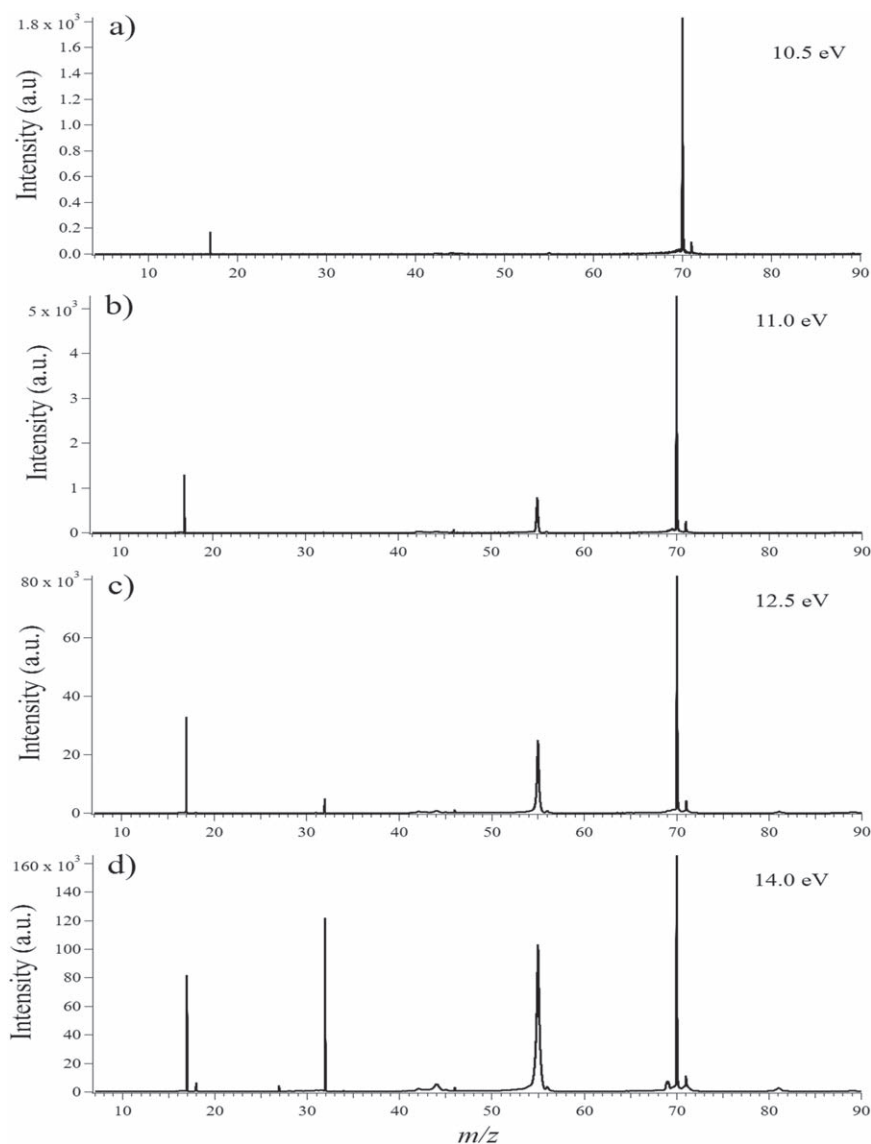
Figure 2. Photoionization mass spectra of 2-APN with ascending energy : (a) hν = 10.5 eV; (b) hν = 11 eV; (c) hν = 12.5 eV; and (d) hν = 14 eV. For discussion, see the text.

The strongest fragment ion is by far m/z 55, formed by methyl (CH$_3$) loss from the 2-APN parent cation. From 11.65 eV on, m/z 55 becomes the strongest ion signal and, at the maximum photon energy of our study, at hν = 14 eV, its intensity is about 70% of all ions. The parent ion itself decreases in intensity with ascending photon energy to attain a value of below 10% of all ions at 14 eV. The other fragment ions (m/z 44, 43, 42, 69) start appearing at approximately 10.5 eV. Their intensities, however, stay quite low throughout the whole energy scan. The m/z 44 mass channel exhibits the highest intensity out of this group, with a maximum of about 10% of all ions, at 14 eV. We can note here already a remarkable difference concerning the fragmentation behavior of 2-APN compared to AAN studied earlier (Bellili et al. 2015a). Whereas in AAN the two dominant fragmentation reactions were loss of H and HCN from the parent ion, in 2-APN there is only one dominant reaction, namely the loss of CH$_3$ via the C–CH$_3$ specific bond breaking. With the help of quantum chemical calculations, it has been shown by Bellili et al. (2015a) that the H atom is abstracted from the α carbon atom (and not from the amino group) of

AAN following photoionization. Thus, for the two molecules, loss of H from AAN$^+$ and CH$_3$ from 2-APN$^+$ will lead to the same stable ion N≡CC(H)NH$_2^+$, which is formally a protonated HCN dimer. HCN dimers are currently discussed as important intermediates on the road to prebiotic building blocks (Melosso et al. 2018; Shingledecker et al. 2020; Sandström & Rahm 2021; Ayachi et al. 2023). This will be further discussed in Section 4.

3.3. SPES of Parent Fragments Ions and Theoretical Calculations

SPES have been recorded in order to get more insight into the involved photoionization dynamics. Figure 4(a) shows the SPES of the parent ion m/z 70, the major fragment ion m/z 55, and the minor ion m/z 69. Up to six electronic bands are observed in this spectrum (numbered with roman numerals from I to VI in Figure 4(a)). The adiabatic ionization energy (AIE) can be found from a zoom on the baseline (not shown) to be AIE$_{exp}$ = 9.85 ± 0.01 eV. This is the value where the ion signal exceeds the background noise, and the given error
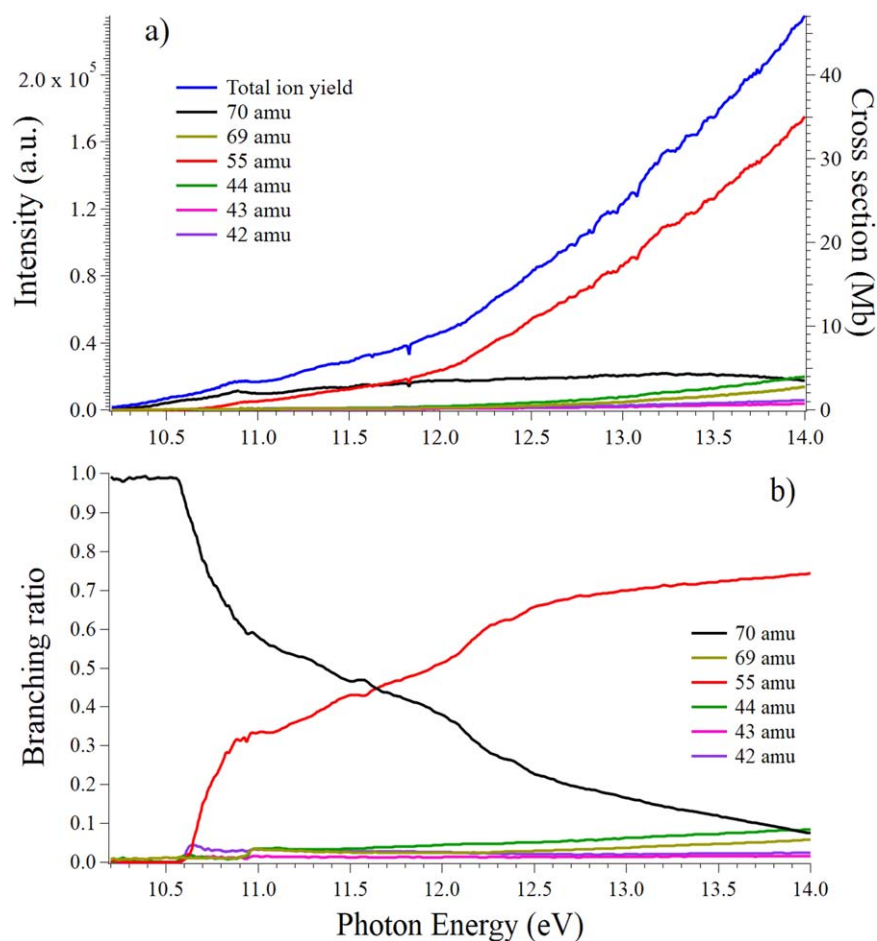
Figure 3. (a) Ion yield spectra of 2-APN in the 10.1–14 eV photon energy range. (b) Branching ratios of the 2-APN parent ion and fragment ions in the 10.3–14 eV photon energy range.

reflects the appreciation of the experimental threshold region. The value determined in this way must be considered as an upper limit. Between 10 and 10.5 eV, the slowly rising m/z 70 ion signal does not represent any pronounced or structured band, as has been found in the SPES of other small molecules of astrophysical interest studied recently (Derbali et al. 2019, 2020). This is due to unfavorable Franck–Condon factors upon 2-APN(X) + $h\nu$ → 2-APN$^+$(X$^+$) + e$^-$ single photon ionization transition. Indeed, in cases where the AIE is not observed as a strong 0–0 transition, one must consider a substantial geometry change between the neutral and parent cation. Briefly, examination of the optimized equilibrium geometries of 2-APN$^+$(X$^+$) and 2-APN(X), as shown in Figure 6, shows that the main changes upon ionization occur in the H$_4$, N$_1$, C$_2$, and H$_5$ part of the molecule, where the H$_4$N$_1$C$_2$ in-plane angle and the H$_4$N$_1$C$_2$H$_5$ dihedral angle exhibit large changes, whereas the bond lengths remain almost unchanged (see also below).

Figure 5 shows calculated and measured AIEs of 2-APN and the appearance energies (AEs) of the different fragmentation pathways. The calculated value of the AIE is found at AIE$_{\text{calc}}$ = 9.59 eV, which is lower than the experimental AIE$_{\text{exp}}$ of 9.85 ± 0.01 eV. The difference of 0.26 eV between both values is not astonishing since appreciable m/z 70 ion intensity appears to be entirely due to ionization outside of the Franck–Condon region, i.e., we are experimentally blind to the true vibrational ground state of the cationic ground state. In such

cases, the true AIEs are difficult or impossible to measure. This effect has been observed in several species, for example most notably in the photoionization of the Ar$_2$ dimer (Briant et al. 2012).

Besides, the 0.26 eV difference can be due to the use of DFT for the computation of the AIE of this medium-sized organic molecule. For instance, in a benchmark study of thymine, some of us (Majdi et al. 2015) showed that a DFT PBE0-based calculated AIE can be lower by ∼0.2 eV from the true value obtained with high accuracy, in this case from high resolution VUV MATI experiments (Choi et al. 2005). To get more accurate calculated AIEs, one often needs the computationally costly explicitly correlated coupled clusters (R)CCSD(T)-F12/cc-pVTZ-F12 approach. This is also confirmed by a study on 3-hydroxyisoquinoline, where we showed that a DFT-based AIE is smaller than the (R)CCSD(T)-F12 and the SPES AIEs by ∼0.23 eV and ∼0.18 eV, respectively (Pan et al. 2013). We note, however, that in the cases of thymine and 3-hydroxyisoquinoline, the 0–0 transitions were Franck–Condon favorable and thus the experimental AIE had been determined with high accuracy by SPES. As stated above, this is not the case here. Thus, for 2-APN, higher levels of theory cannot lead to a conclusive comparison with experiment. In the following, we will recall the PBE0 values for a qualitative assignment of the fragments observed upon dissociative ionization of 2-APN.

Above the AIE, the m/z 70 signal slowly rises to a maximum at $h\nu$ = (10.50 ± 0.02) eV. The maximum of this band (labeled
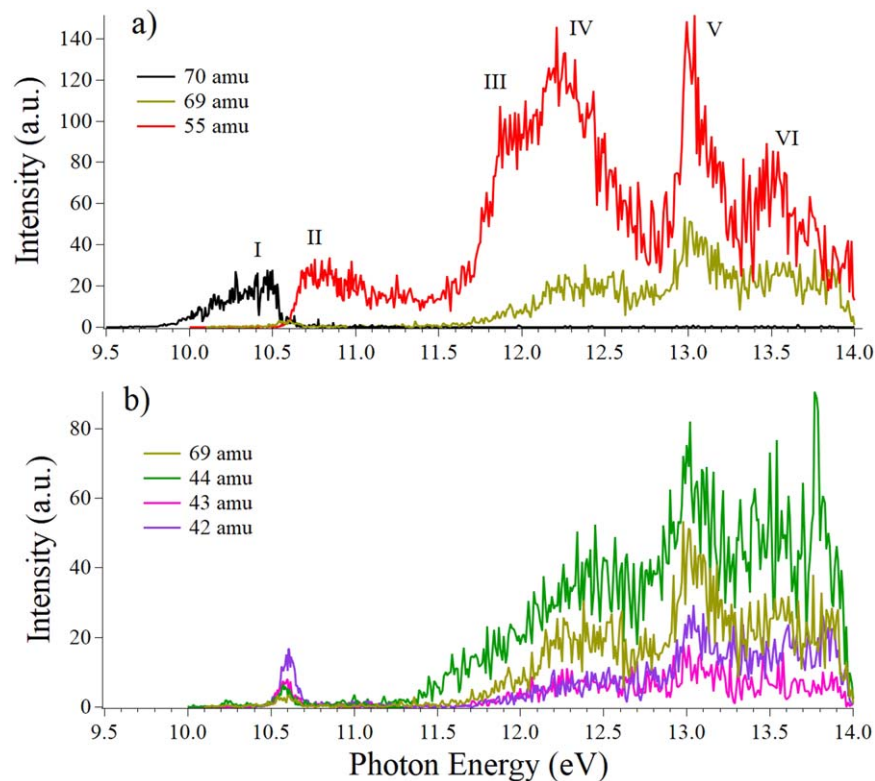
Figure 4. (a) SPES of 2-APN in the 9.5–14 eV photon energy range: parent ion at m/z 70 and fragment ions m/z 55 and m/z 69. (b) SPES of 2-APN in the 10–14 eV photon energy range: fragment ions, m/z 44, m/z 43, m/z 42, and m/z 69.

	Ionization	Dissociative Ionization						
Formula	$C_3H_6N_2^{+\bullet}$	$C_3H_5N_2^+ + H^\bullet$	$C_3H_5N_2^+$ cyclic $+ H^\bullet$	$C_2H_3N_2^+$ linear $+ CH_3^\bullet$	$C_3H_4N^+ + NH_2^\bullet$	$C_2H_6N^+ + CN^\bullet$	$C_2H_5N^{+\bullet}$ "amine" $+ HCN$	$C_2H_5N^{+\bullet}$ "imine" + HCN
Molecular structure of the cationic species								
m/z	70	69	69	55	54	44	43	43
Calc AIE or AE	9.59	10.23	11.11	10.51	12.30	10.59	9.79	10.26
Exptl AIE or AE	9.85 ± 0.01	10.54 ± 0.01	11.65 ± 0.01	10.57 ± 0.01	*Not observed*	10.47 ± 0.01	10.48 ± 0.01 eV	

	Dissociative Ionization						
Formula	$C_2H_4N^+ + CH_2N^\bullet$	$C_2H_4N^+ + HNCH^\bullet$	$C_2H_4N^+ + HCN + H^\bullet$	$C_3H_6^{+\bullet} + N_2$	$CH_2N_2^{+\bullet}$ "NCNH$_2$" isomer $+ C_2H_4$	$CH_2N_2^{+\bullet}$ "NHCNH" isomer $+ C_2H_4$	$CH_2N_2^{+\bullet}$ "CH$_2$N$_2$" isomer $+ C_2H_4$
Molecular structure of the cationic species							
m/z	42			42	42	42	42
Calc AIE or AE	10.57	10.93	11.21	10.89	13.69	13.19	13.45
Exptl AIE or AE	10.48 ± 0.01 eV						

Figure 5. Calculated and measured AIEs of 2-APN and the AEs of the different fragmentation pathways (in eV). The most stable structures that correspond to our experimental results are presented. Cartesian coordinates of optimized structures are given in the Appendix, Tables A1–A22.

"I" in Figure 4(a)), corresponding to the ground state of the 2-APN parent cation, is assigned to its vertical ionization energy (VIE). The ground state slow photoelectron spectrum itself is quite noisy and no distinct rovibronic structure can be recognized within this band, indicating spectral congestion and/or superposition of more discrete vibrational transitions and/or non-Franck–Condon transitions. The absence of a well-pronounced structured band corresponding to the ion's ground state, as well as the large difference between the AIE and VIE (about 0.9 eV considering the calculated AIE value), are
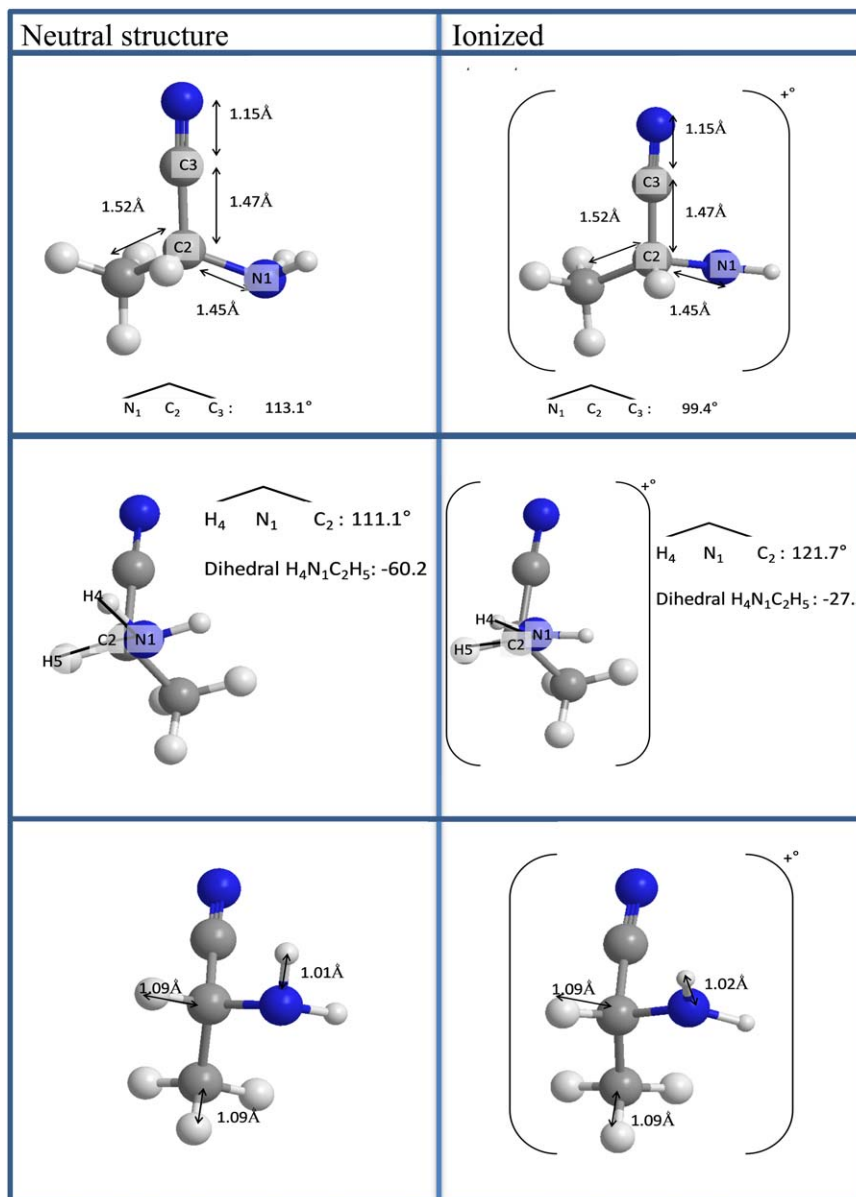
Figure 6. Structural changes arising from ionization of 2-APN in three different spatial views. Left column: neutral 2-APN. Right column: ionized 2-APN.

indicative again of quite different structures of neutral and ionized 2-APN. To corroborate this hypothesis, we present in Figure 6 calculated chemical structures of neutral and ionized 2-APN from three different spatial views. Here, it is shown that bond lengths are quite unchanged; however, we do observe significant bond angle changes. Namely, the N1-C2-C3 angle is reduced from $113°.1$ to $99°.4$, thus by $13°.7$ (see upper row of Figure 6). The H4-N1-C2 angle is increased from $111°.1$ to $121°.7$, thus by $10°.6$ (see middle row of Figure 6). Finally, the dihedral angle H4-N1-C2-H5 is reduced from $-60°.2$ to $-27°.5$ (see middle row of Figure 6). As can be seen from the different viewing angles, the main geometry change occurs around the nitrogen of the amino group (N1), pointing to an ionization of its sp^3 free electron pair orbital. This atom switches to sp^2 hybridization, with a quasiplanar NH_2 structure, as can be seen from Figure 6, transforming it to a form similar to a protonated imine group. The corresponding positive charge located on the N1 atom further implies the attraction of electron density from the central C to the N1 atom. Thus, the dissociation pathway to

an sp^2 hybridized central C to form the all-planar structure of m/z 55 (see below) is already paved.

This substantial geometry change, which can be seen clearly in the three views, is certainly the reason for the large difference between the AIE and the VIE. Several bond angles are changing a lot, and therefore the observed ionization threshold region is well outside the Franck–Condon region. No pronounced AIE band is observed. At the same time, the bond angle changes probably trigger several simultaneous deformation vibrational excitations, with potentially low frequency and many quanta, corroborating the hypothesis of spectral congestion mentioned above.

The intensity of the m/z 70 SPES signal decreases abruptly to zero at 10.5 eV and several dissociative ionization channels open up at this energy, corresponding to the formation of m/z 69, 55, 44, 43, and 42 (see Figures 4(a) and (b)). Apart from m/z 55, these fragments are minor products but curiously appear at nearly the same threshold. Even more curiously, only 0.2 eV above their appearance at approximately 10.7 eV, all dissociation

pathways become dominated by the strongest dissociative photoionization channel, which is the loss of a methyl radical (CH_3), according to $C_3N_2H_6 + h\nu \rightarrow N\equiv CC(H)NH_2^+ + CH_3$. The observed experimental AE of m/z 55 is $AE_{exp} = 10.57 \pm 0.01$ eV. This value is in excellent agreement with our calculations (see Figure 5) yielding $AE_{calc} = 10.51$ eV. This agreement gives us good confidence in the calculated planar structure of m/z 55 shown in Figure 5. As noted above, the structure of the parent cation favors rupture of the C–CH_3 bond, leading to the formation of an sp^2 hybridized central C atom and the formation of the stable $N\equiv CC(H)NH_2^+$ ion.

In the SPES of the m/z 55 mass channel, several excited electronic states can be recognized, giving rise to spectral bands labeled II–VI in Figure 4(a). The nature of these bands will be analyzed in a forthcoming publication, in conjunction with calculations on excited electronic states of the parent molecule and are, as such, out of scope of this work. None of the bands II–VI show a vibrational structure or other resonant features. This could indicate superpositions of vibronic bands and/or spectral congestion of related excited states. However, since we are well above the various dissociation thresholds found at around 10.5 eV, we are confident that we are probing, at least partly, the ionization continuum. In this case, observed band intensities of fragment channels simply reflect their respective reactions rates. The coupling of excited states, either of the parent neutral and the parent cation, with the various observed dissociation channels was not in the focus of this work. This remains to be clarified by forthcoming work.

Figure 4(a) also shows the SPES of m/z 69 formed by hydrogen loss according to $C_3N_2H_6 + h\nu \rightarrow C_3N_2H_5^+ + H$. The experimental AE is found to be $AE_{exp} = 10.54 \pm 0.01$ eV. According to our calculations, abstraction of the H from the central C2 atom leads to $AE_{calc} = 10.23$ eV, which agrees with the experimental value despite a difference of about 0.31 ± 0.01 eV. We can therefore conclude that the m/z 69 ion has a $N\equiv CC(CH_3)NH_2^+$ structure. The intensity of m/z 69 is quite low (see Figure 4), reflecting the low reaction rate of this channel. H abstraction from the central C2 atom is therefore a minor dissociation channel, which agrees with the observation that the methyl loss from the same C2 atom is much faster and dominates by far. We can now easily rationalize the difference between AE_{exp} and AE_{calc}. The latter reflects the thermodynamic threshold, and AE_{exp} is subject to a kinetic shift related to the existence of a potential barrier along this dissociation pathway. This can lead to such a high experimental AE.

In the m/z 69 SPES, a second threshold can be observed, at $AE_{exp} = (11.65 \pm 0.1)$ eV. We propose that, at this energy, the H is abstracted from the methyl group with subsequent cyclization forming the three-membered ring structure shown in Figure 5. The calculated AE for this channel is $AE_{calc} = 11.11$ eV. This is in accordance with the experimental value of the second threshold, considering that, for cyclization reactions, significant activation barriers are common. Hence, the observed experimental AEs are subject to substantial kinetic shifts. Alternatively, we can suggest the formation of the previously identified $N\equiv CC(CH_3)NH_2^+$ isomer but in its electronic excited state. Indeed, the energy difference between both thresholds (∼1.11 eV experimentally) may correspond to the separation of the ground and first excited state in this isomer. At higher energies, the m/z 69 slow photoelectron spectrum follows roughly the same structure observed for m/z

55, indicating that the electronic states that are populated couple to both fragmentation channels.

In the theoretical calculations, we also considered formation of m/z 54 by loss of the amino group, which corresponds to a simple bond rupture from the central C2 atom too. The calculated AE of this ion is 12.3 eV; however, this ion is not observed even at high photon energies. This appears to further confirm that the rupture of the methyl C1-C2 bond is by far dominant in the dissociative ionization of 2-APN.

Figure 4(b) shows SPES of the group of m/z 42, 43, 44, and 69 fragment cations (for the sake of comparison, we show the m/z 69 SPES also in Figure 4(b)). Interestingly, these ions have AEs slightly below that of the main channel, m/z 55. They are all observed in a small window between 10.5 and 10.7 eV but, once the fast m/z 55 channel is open, their contribution to the dissociative ionization is minimized. All four ions have experimental AEs around 10.5 eV (see Figure 5 for exact values) indicating that these channels are all open when populating higher vibrational levels of the cationic ground state. Such a situation was already observed, for instance, during the dissociative single photon ionization of pyruvic acid (Jarraya et al. 2022) via CC bond breaking, where both direct and indirect photoionization processes coupled with fragmentation are in action. Full elucidation of such phenomena requires in-depth treatment of the electronic states of the 2-APN$^+$ cation, which is out of the scope of the present work.

The m/z 44 ion is the strongest at higher energies of this group. It is formed by loss of the CN radical from the central C atom, leaving behind an ion with the elemental formula $C_2H_6N^+$. The structure is given in Figure 5 with $AE_{calc} = 10.59$ eV, in good agreement with the experimental value $AE_{exp} = 10.47 \pm 0.01$ eV.

The m/z 43 ion ($C_2H_5N^+$) is formed by elimination of HCN. Its experimental AE is $AE_{exp} = 10.48 \pm 0.01$ eV. Two ion structures have been considered in the calculations for $C_2H_5N^+$, namely an amine structure $H_3C–C–NH_2^+$, giving $AE_{calc} = 9.79$ eV, and an imine structure $H_3C–CH=NH^+$, yielding $AE_{calc} = 10.26$ eV. In the first case, the HCN elimination involves the H from the central C atom, and in the second case the H atom from the amino group. The latter computation is in better agreement with the experimental value, considering a small kinetic shift, which is expected for this reaction since it is not a simple bond rupture. We therefore assign the imine structure $H_3C–CH=NH^+$ to the m/z 43 ion. We did not consider HNC, hydrogen isocyanide, as a neutral fragment in the calculations since the expected AEs would be even higher by at least +0.65 eV in both cases, given the difference in enthalpy of formation between HCN and HNC (Klippenstein et al. 2017). Furthermore, the elimination of HNC would probably require an even more complicated rearrangement, thereby shifting the AE further toward the blue. HCN loss is a common dissociative ionization reaction in many CN-containing organic molecules; however, in 2-APN, this is only a very minor fragmentation channel.

The m/z 42 ion is the strongest ion in the 10.5–10.7 eV window. In the calculations, several fragmentation pathways have been considered, namely loss of neutrals CH_2N, HCNH, HCN + H, N_2, and C_2H_4 (ethylene). For the elimination of ethylene, three different ion structures have been considered (see Figure 5 for the related results). The experimental AE of m/z 42 is measured to be $AE_{exp} = (10.48 \pm 0.01)$ eV. The loss of methylene amidogen (CH_2N) in connection with the formation of a H_3CCNH^+ structured ion gives the lowest calculated AE of $AE_{calc} = 10.57$ eV of all pathways considered

Table 1
Calculated Photoionization Rates of 2-APN Under Various Radiation Fields and Due to Cosmic-Ray-Induced VUV Photons, Along with the Dissociative Photoionization Rates and Their Relative Contributions to the Total Photoionization Rates Shown in Parentheses, Forming the Two Most Dominant Channels, the Parent Cation (2-APN$^+$) and the m/z 55 (N≡CC(H)NH$_2^+$) Product Channel

Radiation Field	Total Photoionization Rate (s^{-1})	2-APN$^+$ Forming Rate (s^{-1})	N≡CC(H)NH$_2^+$ Forming Rate (s^{-1})
ISRF[a]	2.90E-10	9.30E-11 (32%)	1.58E-10 (54%)
4000 K	2.05E-14	5.57E-15 (27%)	2.06E-15 (10%)
10,000 K	2.47E-11	9.23E-12 (37%)	1.18E-11 (48%)
20,000 K	2.71E-10	7.95E-11 (29%)	1.55E-10 (57%)
Solar	1.02E-11	2.27E-12 (22%)	5.57E-12 (55%)
TW-Hya	9.60E-11	2.88E-11 (30%)	4.10E-11 (43%)
Cosmic ray	2.14E-14	7.16E-15 (33%)	1.10E-14 (51%)

Note.
[a] Interstellar radiation field.

in this study, which is in good agreement with the experimental value. We thus tentatively assign the m/z 42 to the 2-APN + $h\nu$ → CH$_2$N + H$_3$CCNH$^+$ pathway in the 10.5–10.7 eV window. The elimination of N$_2$ would imply the formation of a C$_3$H$_6^+$ radical cation with a relatively low calculated threshold energy (AE$_{calc}$ = 10.89 eV). However, we expect a large kinetic shift for this reaction, which might play a role at higher energies. Elimination of neutral ethylene (C$_2$H$_4$) is a common dissociative photoionization pathway in organic molecules too, given its thermodynamic stability (see, e.g., Klippenstein et al. 2017). We have explored three different corresponding ion structures for the loss of ethylene from the parent cation. All of them have calculated AEs above 13 eV (see Figure 5). These pathways might therefore contribute to the m/z 42 ion intensity in these energy regions.

4. Astrophysical Implications

So far, 2-APN has only been searched for in the Sgr B2(N) complex (Møllendal et al. 2012; Richard et al. 2018). Sgr B2 is the most massive star-forming region in our Galaxy at a projected distance of around 100 pc from the Galactic center and contains two centers of star formation, Sgr B2(N) and Sgr B2(M) (Reid et al. 2009). Both contain ultracompact H II regions, and the star formation rate of Sgr B2 is about 0.04 solar masses annually, which classifies it as a ministarburst (Schmiedeke et al. 2016). More than 70 H II regions have been detected in the whole Sgr B2 cloud complex (Mehringer et al. 1993; Gaume et al. 1995; De Pree et al. 1998), and therefore understanding the effects of ionizing radiation on molecules expected therein is important to place their detections or nondetections in the right context.

Sgr B2 has turned out to be an ideal hunting ground for various organic molecules (Belloche et al. 2013). So far, however, 2-APN has eluded detection on two occasions in the Sgr B2(N) complex, once from observations with the IRAM 30 m telescope (Møllendal et al. 2012) and once with ALMA (Richard et al. 2018), where upper limits were obtained for both 2-APN and its isomer, 3-APN. The two isomers contain a longer carbon chain than AAN, which is well documented in Sgr B2(N). The upper limit abundances of 2-APN and 3-APN derived by Richard et al. (2018) imply that they are at least 5 and 12 times less abundant than AAN. However, the local conditions in Sgr B2(N) may inhibit the survival of 2-APN to some extent given the prevalence of ionizing radiation therein (De Pree et al. 1998).

The α-aminonitrile 2-APN is a molecule with a unique astrophysical and astrobiological relevance. It is the primary product in the Strecker synthesis of α-alanine. The hydrolysis of the cyano group (-CN) in α-aminonitriles gives an organic acid group (-COOH) and thus the amino acid α-alanine in the case of 2-APN. Recent work by Shoji et al. (2023) showed that only the aminonitrile precursors in the Strecker synthesis of amino acids are characterized by enantiomeric excess from circularly polarized (CP) Lyman-α radiation, formed in regions where CP near-infrared light is produced (Fukushima et al. 2023), meaning that homochirality of amino acids is produced at the aminonitrile precursor stage. This is also consistent with nitriles having more extended lifetimes than acids during UV photolysis, so acids (and axiomatically amino acids) could be more rapidly destroyed by photolysis than nitriles in interstellar environments (Bernstein et al. 2004). It is worth noting that it is also possible that amino acids could thermally isomerize to achiral intermediates in environments that are hot and dense enough (Kaur & Vikas 2015). Hence, 2-APN is considered to be a better probe with respect to the detection of α-alanine (Shoji et al. 2023).

By utilizing our scaled photoionization cross section of 2-APN and partial formation cross sections of its two dominant products, namely the 2-APN parent cation (m/z 70) and the m/z 55 fragment ion, assigned to N≡CC(H)NH$_2^+$, we have calculated the photoionization rates in various radiation fields and due to cosmic-ray ionization-induced radiation. The chosen photon energy range in the experiment (from threshold to 14 eV or 88 nm) encompasses the fluxes of the radiation fields to accurately derive the photorates in the presented radiation fields. These photorates are calculated in a manner that has been described very recently in detail (Hrodmarsson & van Dishoeck 2023). The computed rates are presented in Table 1. When these photoionization rates for 2-APN are compared to the photoionization rates of other complex organic molecules, such as dimethyl ether (DME) and acetaldehyde (AA) (see Hrodmarsson & van Dishoeck 2023), they appear to be a factor of a few to an order of magnitude smaller than those in DME and AA, and of similar value as those of methyl formate. Since our scaling should be considered preliminary and only accurate to within an order of magnitude, it is difficult to conclude whether this verifies the previous verdict by Bernstein et al. (2004) that CN-containing molecules are more photostable.

The most stable isomer of the C$_3$H$_6$N$_2$ family is found to be 2-APN (Shoji et al. 2022). Thus, in accordance with the MEP, it is expected that 2-APN should be the easiest member of the C$_3$H$_6$N$_2$ family to be detected, with 3-APN following closely.

While this appears consistent with searches for 2-APN and 3-APN (see Richard et al. 2018), multiple discrepancies can exist between observations of isomers and the MEP. This has been highlighted recently with notable examples such as the C_2H_3O (Shingledecker et al. 2019), the C_3H_4O (Fuentetaja et al. 2023), and the $C_2H_2N_2$ (Shingledecker et al. 2020) isomer families.

In our study, we have found that dissociative photoionization of 2-APN overwhelmingly gives rise to the loss of methyl (CH_3). This simple bond rupture reaction yields a planar isomer of the $C_2H_3N_2^+$ family, with a $N{\equiv}CC(H)NH_2^+$ structure, as confirmed by our calculations. The ease of formation of this ion in the dissociative photoionization of 2-APN affirms its thermodynamic stability. $N{\equiv}CC(H)NH_2^+$ corresponds to a protonated version of low-lying HCN dimers (Smith et al. 2001). It can also be regarded as protonated cyanomethanimine. The latter molecule, formally a dimer of HCN too, has been detected by Zaleski et al. (2013). HCN dimers are astrobiologically highly relevant since they are potential precursors to more complex prebiotic species such as adenine (Oró 1961; Chakrabarti & Chakrabarti 2000). Interestingly, in AAN, the same ion is formed, namely by loss of an H atom from the central C atom of the ionized parent molecule $N{\equiv}CCH_2NH_2$, also verified by quantum chemical calculations on its structure (Bellili et al. 2015a). Similarly, in the dissociative photoionization of AAN, $N{\equiv}CC(H)NH_2^+$ is the strongest fragment ion formed too, among six other ions formed. Hence, while 2-APN is indeed considered to be a viable probe of the amino acid alanine, and likewise AAN of glycine, their interaction with ionizing radiation has the capacity to link them to precursors of prebiotic species like the DNA base adenine. This type of photodestruction could contribute to the lack of detections of 2-APN in Sgr B2(N), but further searches for HCN dimers and their protonated forms could shed further light on the chemistry of complex aminonitrile molecules in space.

5. Conclusion

We have studied the single photoionization and dissociative photoionization of 2-aminopropionitrile ($C_3H_6N_2$; 2-APN) in the 9–14 eV energy range using tunable synchrotron radiation in conjunction with electron/ion coincidence spectroscopy. The experimental results were analyzed with the help of first principles calculations. The chiral 2-APN is a molecule of considerable interest in astrochemistry and astrobiology, as has been outlined above; however, it has not yet been detected in astrophysical objects despite several radioastronomical searches. Its interaction with VUV radiation has been studied here in order to rationalize its nondetection. The experimental AIE has been determined to be AIE = (9.85 ± 0.01) eV. To the best of our knowledge, the ionization energy of 2-APN was unknown before. However, this value has to be considered as an upper limit, since a pronounced 0–0 transition is not observed in our study. This is explained by a considerable geometry difference between neutral 2-APN and its corresponding cation, as demonstrated by our structural calculations.

Photoion yield spectra have been measured and calibrated to absolute photoionization cross sections. From this, photoionization and ion formation rates have been calculated for typical interstellar radiation fields and cosmic-ray ionization. Besides the parent cation ($C_3H_6N_2^+$; m/z 70), m/z 55 is the major

fragment ion, with a yield of about 70% at photon energies above 12.5 eV. Our calculations allowed us to assign the structure of this ion to be $N{\equiv}CC(H)NH_2^+$, being formed by loss of the methyl group from the parent ion. Interestingly, the same ion is formed by dissociative photoionization of aminoacetonitrile ($C_2H_4N_2$; Bellili et al. 2015a), also with very high yield. α-aminonitriles are precursors of amino acids. AAN and 2-APN can furthermore yield efficiently the protonated HCN dimers $N{\equiv}CC(H)NH_2^+$ upon ionization by VUV radiation. HCN dimers are considered to be precursors of DNA bases space and thus aminonitriles appear to be molecules that can give rise to two classes of important biomolecules.

Other ions are formed too in the dissociative photoionization of 2-APN, with low yield, however. These are $H_3C(NH_2)CN^+$ (m/z 69), $CH_3CHNH_2^+$ (m/z 44), CH_3CHNH^+ (m/z 43), and CH_3CNH^+ (m/z 42). All chemical structures are confirmed by theoretical computations of the measured AEs. All fragment ions, especially the main one $N{\equiv}CC(H)NH_2^+$, can be tracers of 2-APN in interstellar objects where large molecules prevail.

Appendix
Cartesian Coordinates of Optimized Structures

Cartesian coordinates of optimized structures are given in Tables A1–A22 together with their energies calculated at the PBE0/aug-cc-pVTZ level. The theoretical procedure is detailed in Section 2 of the article.

Table A1
Neutral 2-APN

N	0.982557	1.263003	−0.118372
H	0.908618	1.296480	−1.127828
C	0.379472	0.045249	0.394204
H	0.470490	0.064719	1.484337
C	1.115852	−1.177265	−0.134845
H	2.166460	−1.105677	0.144347
H	0.694159	−2.095629	0.273024
H	1.045306	−1.224969	−1.223169
C	−1.061560	−0.057233	0.096597
N	−2.182774	−0.103354	−0.157443
H	0.513901	2.083032	0.244252

Sum of electronic and ZPE[a] (harmonic, Hartree)	−227.1347828
Total Anharm (eV)	2.465771133

Note.
[a] Zero point energy.

Table A2
Parent Ion $C_3H_6N_2^{+\cdot}$, m/z 70

N	0.564790	1.344826	−0.147787
H	0.741512	1.440534	−1.148572
C	0.409222	0.027336	0.438967
H	0.526442	0.120432	1.522005
C	1.351682	−0.998971	−0.164784
H	2.383483	−0.735082	0.065465
H	1.130348	−1.969037	0.280383
H	1.216094	−1.079972	−1.244075
C	−1.007720	−0.209184	0.125421
N	−2.115988	−0.328377	−0.173111
H	0.341404	2.192893	0.373454
Sum of electronic and ZPE (harmonic, Hartree)			−226.7823727
Total Anharm (eV)			2.403951287

Table A3
$C_3H_5N_2^+$, m/z 69, Linear Structure

C	−1.189675	−1.163203	−0.000087
C	−0.372238	0.069896	−0.000001
C	1.060464	−0.032722	0.000249
N	−0.886214	1.253796	−0.000110
N	2.215588	−0.147017	0.000070
H	−2.254926	−0.943475	−0.000741
H	−0.922183	−1.755691	0.878630
H	−0.921193	−1.756304	−0.878075
H	−0.305299	2.086717	−0.000075
H	−1.893331	1.377479	−0.000422
Sum of electronic and ZPE (harmonic, Hartree)			−226.2566268
Total Anharm (eV)			2.160815645

Table A4
$C_3H_5N_2^+$, m/z 69, Cyclic Structure

C	1.229766	−0.742816	−0.255564
C	0.193092	−0.113463	0.590241
C	−1.167216	−0.039224	0.141429
N	1.161584	0.734100	−0.172185
N	−2.247578	0.022818	−0.242522
H	2.097802	−1.176183	0.222786
H	0.945932	−1.143229	−1.219766
H	0.348881	−0.082067	1.663105
H	0.801884	1.244783	−0.974410
H	1.873604	1.231288	0.354596
Sum of electronic and ZPE (harmonic, Hartree)			−226.2255411
Total Anharm (eV)			2.237105349

Table A5
$C_2H_3N_2^+$, m/z 55

N	1.505847	−0.328477	−0.000302
C	0.536698	0.506046	0.000235
C	−0.812137	0.089679	0.000512
N	−1.923400	−0.215267	−0.000341
H	1.350032	−1.333911	0.000827
H	2.469603	−0.006487	−0.000108
H	0.755861	1.572255	−0.000696
Sum of electronic and ZPE (harmonic, Hartree)			−186.9791669
Total Anharm (eV)			1.429613071

Table A6
CH_3°

C	0.000109	−0.000001	−0.000086
H	−0.544016	−0.932567	0.000171
H	−0.536305	0.937020	0.000171
H	1.079667	−0.004448	0.000171
Sum of electronic and ZPE (harmonic, Hartree)			−39.7695721
Total Anharm (eV)			0.801320586

Table A7
$C_3H_4N_2^+$, m/z 54

C	−0.466781	0.525806	−0.000009
C	−1.591136	−0.347604	−0.000002
C	0.853092	0.097467	−0.000045
N	1.959911	−0.253119	0.000027
H	−0.618706	1.607965	0.000059
H	−2.246462	−0.039453	0.842815
H	−2.246625	−0.039308	−0.842632
H	−1.378633	−1.411380	−0.000094
Sum of electronic and ZPE (harmonic, Hartree)			−170.9270082
Total Anharm (eV)			1.641998689

Table A8
NH_2°

N	0.000000	0.000000	0.141593
H	0.000000	0.803298	−0.495577
H	0.000000	−0.803298	−0.495577
Sum of electronic and ZPE (harmonic, Hartree)			−55.8171548
Total Anharm (eV)			0.514707188

Table A9
$C_2H_6N^+$, m/z 44

N	1.183684	−0.200719	−0.000056
C	0.081580	0.450387	0.000037
C	−1.237329	−0.170206	0.000022
H	1.199992	−1.215164	−0.000155
H	2.080424	0.271311	−0.000034
H	0.164510	1.535288	0.000138
H	−1.793561	0.195356	0.871108
H	−1.793668	0.195598	−0.870891
H	−1.208991	−1.258443	−0.000125
Sum of electronic and ZPE (harmonic, Hartree)			−134.1192473
Total Anharm (eV)			2.210518153

Table A10
CN°

N	0.000000	0.000000	0.535538
C	0.000000	0.000000	−0.624795
Sum of electronic and ZPE (harmonic, Hartree)			−92.6313587
Total Anharm (eV)			0.134730874

Table A11
$C_2H_5N^{+\circ}$ "Amine," m/z 43

N	−1.239002	0.092450	0.000042
C	−0.073943	−0.386872	−0.000098
C	1.278732	0.089092	−0.000050
H	−1.421348	1.098934	−0.000220
H	−2.056412	−0.514538	0.000070
H	1.793556	−0.313960	0.879595
H	1.794821	−0.315473	−0.878155
H	1.333664	1.184568	−0.000700

Sum of electronic and ZPE (harmonic, Hartree)	−133.4480395
Total Anharm (eV)	1.815019514

Table A12
HCN

C	0.000000	0.000000	−0.496542
N	0.000000	0.000000	0.649083
H	0.000000	0.000000	−1.564327

Sum of electronic and ZPE (harmonic, Hartree)	−93.3270983
Total Anharm (eV)	0.442103516

Table A13
$C_2H_5N^{+\circ}$ "Imine," m/z 43

N	−1.240117	−0.149803	−0.000060
C	−0.162672	0.450559	−0.000012
C	1.181637	−0.203553	−0.000068
H	−1.767134	−1.018758	0.000199
H	−0.212798	1.549051	0.000207
H	1.713447	0.162759	−0.883768
H	1.712580	0.161675	0.884707
H	1.120928	−1.288135	−0.000445

Sum of electronic and ZPE (harmonic, Hartree)	−133.4306005
Total Anharm (eV)	1.751533069

Table A14
$C_2H_4N^+$, m/z 42

C	1.262112	−0.000062	−0.000013
C	−0.165808	0.000140	0.000208
N	−1.302891	−0.000142	−0.000129
H	1.618288	0.501099	0.904815
H	1.617363	0.533412	−0.886558
H	1.617720	−1.034400	−0.018850
H	−2.310952	0.000416	0.000322

Sum of electronic and ZPE (harmonic, Hartree)	−132.9509208
Total Anharm (eV)	1.504636678

Table A15
$CH_2N^{\bullet}$

N	−0.094270	0.026786	−0.711986
C	0.075973	−0.116173	0.505141
H	0.144965	−1.113155	0.959331
H	0.164331	0.748543	1.175514

Sum of electronic and ZPE (harmonic, Hartree)	−93.876820
Total Anharm (eV)	0.676461457

Table A16
$HNCH^{\bullet}$

N	0.555448	−0.173879	0.000008
C	−0.614650	0.192049	0.000012
H	1.288744	0.533132	−0.000063
H	−1.488978	−0.468276	−0.000063

Sum of electronic and ZPE (harmonic, Hartree)	−93.864328
Total Anharm (eV)	0.695091444

Table A17
$CH_2N_2^{+\bullet}$, "NCNH$_2$" Isomer; m/z 42

N	−1.084547	−0.000005	0.000009
C	0.190233	0.000087	0.000192
N	1.380725	−0.000024	−0.000100
H	−1.607566	0.879888	−0.000255
H	−1.607083	−0.880209	−0.000255

Sum of electronic and ZPE (harmonic, Hartree)	−148.257666
Total Anharm (eV)	0.888304679

Table A18
C_2H_4

C	0.000000	0.661613	0.000016
C	0.000000	−0.661613	0.000016
H	0.922808	1.230369	−0.000049
H	−0.922787	1.230394	−0.000050
H	−0.922808	−1.230369	−0.000049
H	0.922787	−1.230394	−0.000050

Sum of electronic and ZPE (harmonic, Hartree)	−78.460981
Total Anharm (eV)	1.372079838

Table A19
$CH_2N_2^{+\bullet}$ "NHCNH" Isomer, m/z 42

N	1.200991	−0.122378	0.000081
C	−0.000000	0.000032	−0.000195
N	−1.200992	0.122355	0.000081
H	1.996233	0.515318	0.000018
H	−1.996223	−0.515352	0.000018

Sum of electronic and ZPE (harmonic, Hartree)	−148.268177
Total Anharm (eV)	0.754224727

Table A20
$CH_2N_2^{+\bullet}$ "CH$_2$NN" Isomer, m/z 42

C	1.154766	0.000014	0.000001
N	−0.175034	−0.000025	0.000000
N	−1.284880	0.000016	−0.000000
H	1.645382	−0.968939	−0.000003
H	1.645422	0.968922	−0.000003

Sum of electronic and ZPE (harmonic, Hartree)	−148.262195
Total Anharm (eV)	0.842473212

Table A21
$C_3H_6^{+\bullet}$, m/z 42

C	−1.204458	−0.199409	−0.004771
C	0.072179 0.460122 0.003371		
C	1.312946	−0.208655	−0.000507
H	−1.812936	0.205596	−0.834344
H	−1.171689	−1.285037	−0.028791
H	−1.787324	0.163617	0.864214
H	0.088022	1.548674	0.015260
H	2.243494 0.347956	−0.031974	
H	1.356432	−1.293155	0.027079
Sum of electronic and ZPE (harmonic, Hartree)		−117.372143
Total Anharm (eV)		1.86020971

Table A22
N_2

N	−0.000000	−0.000000	0.544956
N	0.000000	−0.000000	−0.544956
Sum of electronic and ZPE (harmonic, Hartree)		−109.437624
Total Anharm (eV)		0.153314659

ORCID iDs

Helgi Rafn Hrodmarsson https://orcid.org/0000-0002-9613-5684
Martin Schwell https://orcid.org/0000-0002-7568-190X
Nicolas Fray https://orcid.org/0000-0002-9140-5462
Jean-Claude Guillemin https://orcid.org/0000-0002-2929-057X
Majdi Hochlaf https://orcid.org/0000-0002-4737-7978
Emilie-Laure Zins https://orcid.org/0000-0002-2157-6696

References

Adamo, C., & Barone, V. 1999, JChPh, 110, 6158
Agúndez, M., Cernicharo, J., de Vicente, P., et al. 2015, A&A, 579, L10
Askeland, E., Møllendal, H., Uggerud, E., et al. 2006, JPCA, 110, 12572
Ayachi, H., Gazzeh, H., Boubaker, T., & Guillemin, J.-C. 2023, J. Org. Chem., 88, 2570
Baer, T., & Tuckett, R. P. 2017, PCCP, 19, 9698
Bailey, J. 1998, Sci, 281, 672
Bejaud, M., Mion, L., Taillades, J., & Commeyras, A. 1975, Tetrahedron, 31, 403
Bellili, A., Gouid, Z., Gazeau, M. C., et al. 2019, PCCP, 21, 26017
Bellili, A., Schwell, M., Bénilan, Y., et al. 2014, JChPh, 141, 134311
Bellili, A., Schwell, M., Bénilan, Y., et al. 2015a, JMoSp, 315, 196
Bellili, A., Linguerri, R., Hochlaf, M., & Puzzarini, C. 2015b, JChPh, 143, 184314
Belloche, A., Menten, K. M., Comito, C., et al. 2008, A&A, 482, 179
Belloche, A., Müller, H. S. P., Menten, K. M., Schilke, P., & Comito, C. 2013, A&A, 559, A47
Bernstein, M. P., Ashbourn, S. F. M., Sandford, S. A., & Allamandola, L. J. 2004, ApJ, 601, 365
Bonner, W. A. 1995, OLEB, 25, 175
Briant, M., Poisson, L., Hochlaf, M., et al. 2012, PhRvL, 109, 193401
Burkhardt, A. M., Lee, K. L. K., Changala, P. B., et al. 2021, ApJL, 913, L18
Cernicharo, J., Agúndez, M., Cabezas, C., et al. 2021, A&A, 649, L15
Chakrabarti, S., & Chakrabarti, S. K. 2000, A&A, 354, L6
Choi, K. W., Lee, J. H., & Kim, S. K. 2005, JACS, 127, 15674
Cole, G. C., Møllendal, H., Khater, B., & Guillemin, J.-C. 2007, JPCA, 111, 1259
Cunningham, M. R., Jones, P. A., Godfrey, P. D., et al. 2007, MNRAS, 376, 1201
de Marcellus, P., Meinert, C., Nuevo, M., et al. 2011, ApJL, 727, L27
De Pree, C. G., Goss, W. M., & Gaume, R. A. 1998, ApJ, 500, 847

Derbali, I., Hrodmarsson, H. R., Gouid, Z., et al. 2019, PCCP, 21, 14053
Derbali, I., Hrodmarsson, H. R., Schwell, M., et al. 2020, PCCP, 22, 20394
Dunning, T. H., Jr. 1989, JChPh, 90, 1007
Ellinger, Y., Pauzat, F., Markovits, A., Allaire, A., & Guillemin, J.-C. 2020, A&A, 633, A49
Endres, C. P., Schlemmer, S., Schilke, P., Stutzki, J., & Müller, H. S. P. 2016, JMoSp, 327, 95
Ernzerhof, M., & Scuseria, G. E. 1999, JChPh, 110, 5029
Evans, A. C., Meinert, C., Giri, C., Goesmann, F., & Meierhenrich, U. J. 2012, Chem. Soc. Rev., 41, 5447
Fuentetaja, R., Bermúdez, C., Cabezas, C., et al. 2023, A&A, 671, L6
Fukue, T., Tamura, M., Kandori, R., et al. 2010, OLEB, 40, 335
Fukushima, H., Yajima, H., & Umemura, M. 2023, MNRAS, 524, 2114
Garcia, G., Nahon, L., & Powis, I. 2004, RScI, 75, 4989
Garcia, G. A., de Miranda, B. K. C., Tia, M., Daly, S., & Nahon, L. 2013, RScI, 84, 053112
Gaume, R. A., Claussen, M. J., de Pree, C. G., Goss, W. M., & Mehringer, D. M. 1995, ApJ, 449, 663
Guijarro, A., & Yus, M. 2007, The Origin of Chirality in the Molecules of Life (Cambridge: RSC Publishing)
Guillemin, J.-C., & Denis, J. 1988, Tetrahedron, 44, 4431
Hatano, Y. 1999a, Radiat. Environ. Biophys., 38, 239
Hatano, Y. 1999b, PhR, 313, 110
Hatano, Y. 2001, JESRP, 119, 107
Hrodmarsson, H. R., Garcia, G. A., Nahon, L., Loison, J.-C., & Gans, B. 2019, JPCA, 123, 9193
Hrodmarsson, H. R., & van Dishoeck, E. F. 2023, A&A, 675, A25
Jarraya, M., Bellili, A., Barreau, L., et al. 2022, FaDi, 238, 266
Jones, P. A., Cunningham, M. R., Godfrey, P. D., & Cragg, D. M. 2007, MNRAS, 374, 579
Kaur, R., & Vikas 2015, JChPh, 142, 074307
Kendall, R. A., Dunning, T. H., Jr., & Harrison, R. J. 1992, JChPh, 96, 6796
Klippenstein, S. J., Harding, L. B., & Ruscic, B. 2017, JPCA, 121, 6580
Lattelais, M., Pauzat, F., Ellinger, Y., & Ceccarelli, C. 2009, ApJL, 696, L133
Lattelais, M., Pauzat, F., Ellinger, Y., & Ceccarelli, C. 2010, A&A, 519, A30
Majdi, Y., Hochlaf, M., Pan, Y., et al. 2015, JPCA, 119, 5951
Marcouille, O., Brunelle, P., Chubar, O., et al. 2007, in AIP Conf. Proc. 879, Synchrotron Radiation Instrumentation: Ninth Int. Conf. on Synchrotron Radiation Instrumentation, ed. J.-Y. Choi & S. Rah (Melville, NY: AIP), 311
Mason, S. 1986, Trends Pharmacol. Sci., 7, 20
McGuire, B. A., Carroll, P. B., Loomis, R. A., et al. 2016, Sci, 352, 1449
McGuire, B. A., Loomis, R. A., Burkhardt, A. M., et al. 2021, Scie, 371, 1265
Mehringer, D. M., Palmer, P., Goss, W. M., & Yusef-Zadeh, F. 1993, ApJ, 412, 684
Melosso, M., Melli, A., Puzzarini, C., et al. 2018, A&A, 609, A121
Møllendal, H., Margulès, L., Belloche, A., et al. 2012, A&A, 538, A51
Nahon, L., de Oliveira, N., Garcia, G. A., et al. 2012, JSynR, 19, 508
Nuevo, M., Meierhenrich, U. J., Muñoz Caro, G. M., et al. 2006, A&A, 457, 741
Oró, J. 1961, Natur, 191, 1193
Pan, Y., Lau, K.-C., Poisson, L., et al. 2013, JPCA, 117, 8095
Perdew, J. P., Burke, K., & Ernzerhof, M. 1996, PhRvL, 77, 3865
Perdew, J. P., Burke, K., & Ernzerhof, M. 1997, PhRvL, 78, 1396
Ponnamperuma, C., & Woeller, F. 1967, Curr. Mod. Biol., 1, 156
Poully, J. C., Schermann, J. P., Nieuwjaer, N., et al. 2010, PCCP, 12, 3566
Reid, M. J., Menten, K. M., Zheng, X. W., Brunthaler, A., & Xu, Y. 2009, ApJ, 705, 1548
Richard, C., Belloche, A., Margulès, et al. 2018, JMoSp, 345, 51
Rivilla, V. M., Sanz-Novo, M., Jiménez-Serra, I., et al. 2023, ApJL, 953, L20
Ruede, R., Troxler, H., Beglinger, C., & Jungen, M. 1993, CPL, 203, 477
Samson, J. A. R., Haddad, G. N., & Kilcoyne, L. D. 1987, JChPh, 87, 6416
Sandström, H., & Rahm, M. 2021, ECS, 5, 2152
Schmiedeke, A., Schilke, P., Möller, Th., et al. 2016, A&A, 588, A143
Shingledecker, C. N., Álvarez-Barcia, S., Korn, V. H., & Kästner, J. 2019, ApJ, 878, 80
Shingledecker, C. N., Molpeceres, G., Rivilla, V. M., Majumdar, L., & Kästner, J. 2020, ApJ, 897, 158
Shoji, M., Kitazawa, Y., Sato, A., et al. 2023, JPCL, 14, 3243
Shoji, M., Watanabe, N., Hori, Y., et al. 2022, AsBio, 22, 1129
Smith, I. W. M., Talbi, D., & Herbst, E. 2001, A&A, 369, 611
Snyder, L. E., Lovas, F. J., Hollis, J. M., et al. 2005, ApJ, 619, 914
Takano, Y., Takahashi, J., Kaneko, T., Marumo, K., & Kobayashi, K. 2007, E&PSL, 254, 106
Tang, X., Garcia, G. A., Gil, J.-F., & Nahon, L. 2015, RScI, 86, 123108
Zaleski, D. P., Seifert, N. A., Steber, A. L., et al. 2013, ApJL, 765, L10